Multimodal aeroelastic analysis of suspension bridges with aerostatic nonlinearities

Journal of Physics: Conference Series **2647** (2024) 242006 doi:10.1088/1742-6596/2647/24/242006

Multimodal aeroelastic analysis of suspension bridges with aerostatic nonlinearities

S Russo, G Piana and A Carpinteri

Dept. of Structural, Geotechnical and Building Eng.ng, Polytechnic University of Turin, Corso Duca degli Abruzzi 24, Turin 10129, Italy

sebastiano.russo@polito.it

Abstract. A one-dimensional (1D) continuum model for the multimodal aeroelastic analysis of suspension bridges is presented which refines a previous model by some of the authors. The classical linearized equations governing the (self-excited) bridge vertical and torsional oscillations are enhanced to include geometric stiffness contributions related to the steady lift and drag forces. A multi-degree-of-freedom (MDOF) system is obtained by Galerkin method and, for increasing values of wind speed, the damped linear dynamics, modulated by both the steady and the self-excited aerodynamic forces, is studied in the complex field. Stability thresholds for divergence and flutter are determined by the classical Lyapunov dynamic criterion. Selected engineering case studies are considered to demonstrate the capabilities and the validity of the proposed model and of the relevant numerical code. In a comprehensive dynamic framework, the method allows for: (i) determining the variation of the bridge mode shapes and frequencies for increasing values of wind speed, including an effective description of the coupling between the two displacement components as well as the interaction between different vibration modes; (ii) detecting both single-degree-of-freedom (i.e. damping-driven) and coupled (i.e. stiffness-driven) flutter instability; (iii) detecting static divergence instability; and (iv) investigating geometric nonlinearities associated with the aerostatic load.

1. Introduction

Aeroelastic stability is one of the main concerns in the design of long-span suspension bridges. Suspension bridges subjected to self-excited aerodynamic load represent a dynamic non-proportionally damped system where both damping and stiffness are affected by wind load and oscillation frequency.

Here, we present a 1D continuum model for the multimodal aeroelastic analysis of suspension bridges which refines a previous model by some of the authors [1]. The equations governing the bridge vertical and torsional motion, based on the classical linearized theory, are enhanced to include the following wind-related geometric nonlinearities: the stiffening/softening induced by the upward/downward lift force and a Prandtl-like second-order effect due to the drag force. For this purpose, the linearization of the equilibrium equations is made around the preloaded bridge configuration under the dead load and the mean steady drag and lift forces. The unsteady component of the wind load, defined via Scanlan's flutter derivatives, is embedded as a self-excited perturbation of the preloaded system. According to the model, the coupling between vertical and torsional motion is triggered by the static wind load, in addition to the coupling provided by the unsteady aerodynamic load already included in classical flutter theories.

Two notable engineering cases are selected to demonstrate the model capabilities.

2. 1D continuum model with aerostatic nonlinearities

We consider the undeformed configuration preloaded by the dead load plus static lift and drag forces (figure 1a), and a perturbed configuration under preloading effects plus self-excited lift and moment (figure 1b).

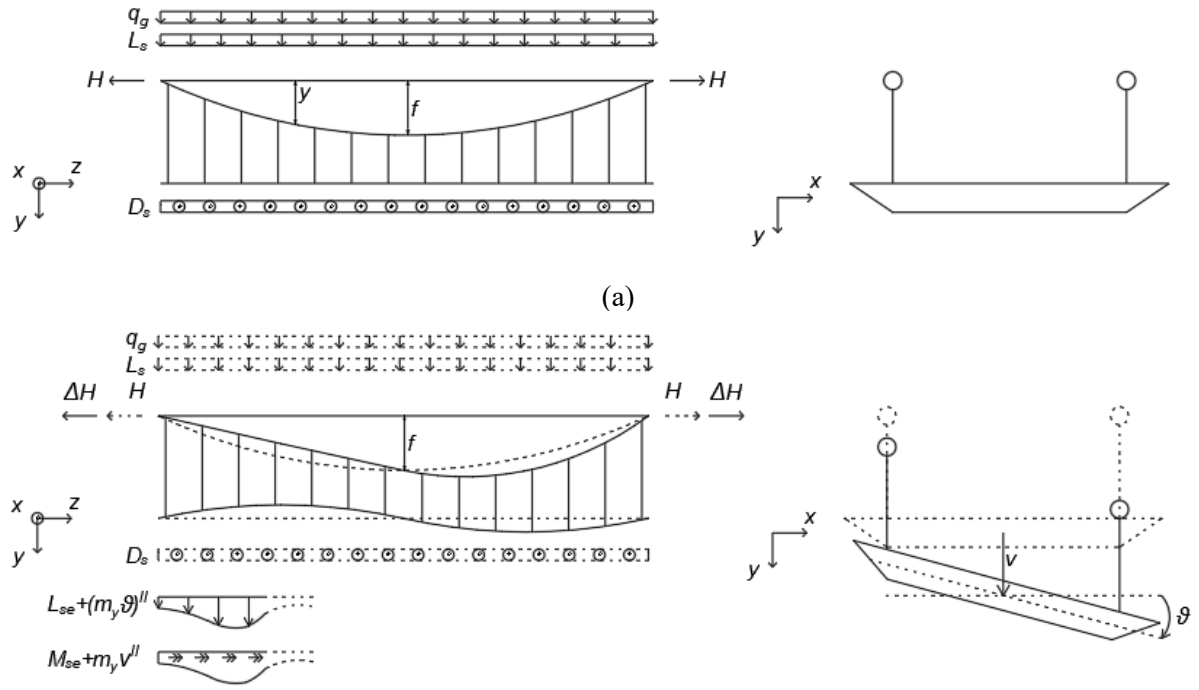

Figure 1. (a) Undeformed configuration preloaded by dead load plus aerostatic lift and drag forces. (b) Perturbed configuration under preloading effects plus self-excited lift and moment actions.

Vertical and torsional oscillations of the suspension bridge subjected to aeroelastic loads are governed by the following equations, in which the drag force is embedded as a Prandtl-like effect [1]:

$$\mu_g \frac{\partial^2 v(z,t)}{\partial t^2} + c_v \frac{\partial v(z,t)}{\partial t} + EI_x \frac{\partial^4 v(z,t)}{\partial z^4} - H \frac{\partial^2 v(z,t)}{\partial z^2} + \frac{\partial^2 \left(m_y(z)\vartheta(z,t)\right)}{\partial z^2} + \left(\frac{8f}{l}\right)^2 \frac{E_c A_c}{L_c} \int_0^l v(z,t)dz = L_{se} \tag{1}$$

$$I_\vartheta \frac{\partial^2 \vartheta(z,t)}{\partial t^2} + c_\vartheta \frac{\partial \vartheta(z,t)}{\partial t} + EI_\omega \frac{\partial^4 \vartheta(z,t)}{\partial z^4} - (GI_t + Hb^2) \frac{\partial^2 \vartheta(z,t)}{\partial z^2} + m_y(z) \frac{\partial^2 v(z,t)}{\partial z^2} + b^2 \left(\frac{8f}{l}\right)^2 \frac{E_c A_c}{L_c} \int_0^l \vartheta(z,t)dz = M_{se} \tag{2}$$

where: v and ϑ are the vertical and torsional displacement of the deck cross-section; μ_g and I_ϑ are the bridge mass and mass moment of inertia per unit length; $c_v = 2\mu_g \xi_v \omega_v$ and $c_\vartheta = 2I_\vartheta \xi_\vartheta \omega_\vartheta$ are damping coefficients, being ξ_v, ξ_ϑ and $\omega_v, \omega_\vartheta$ damping ratios and angular frequencies; EI_x, EI_ω and GI_t are the vertical bending rigidity, warping and primary torsional rigidity, respectively; H is the

horizontal component of the main cables tension; l is the main span length; b is half the distance between cables; f, L_c, A_c and E_c are the cable sag, length, cross-section area and Young modulus; L_{ae} and M_{ae} are the aeroelastic (self-excited) lift and moment; $m_y(z)$ is the horizontal bending moment due to the steady drag force.

Static (subscript *s*) and self-excited (subscript *se*) forces are defined as follows, where for the latter the classic Scanlan definition is adopted [2]:

$$D_s = \frac{1}{2}\rho U^2 B C_{d,0} \tag{3}$$

$$L_s = \frac{1}{2}\rho U^2 B C_{l,0} \tag{4}$$

$$L_{se} = \frac{1}{2}\rho U^2 B \left(K H_1^* \frac{\dot{v}}{U} + K H_2^* \frac{B\dot{\vartheta}}{U} + K^2 H_3^* \vartheta + K^2 H_4^* \frac{v}{B} \right) \tag{5}$$

$$M_{se} = \frac{1}{2}\rho U^2 B^2 \left(K A_1^* \frac{\dot{v}}{U} + K A_2^* \frac{B\dot{\vartheta}}{U} + K^2 A_3^* \vartheta + K^2 A_4^* \frac{v}{B} \right) \tag{6}$$

being: ρ the air density; U the wind speed; B the cross-section width; $C_{d,0}$ and $C_{l,0}$ the static drag and lift coefficients at zero angle of attack; $K = \omega B/U$ the reduced frequency; and H_i^*, A_i^* with $i = 1,2,3,4$ are the flutter derivatives of the cross-section. The proposed continuum model, easily allows to account for the variation of flutter derivatives along longitudinal bridge axis, just by replacing constant values of flutter derivatives by their respective span-wise functions.

2.1. Aerostatic nonlinearities

Drag force per unit span length induces a bending moment in the horizontal plane, which satisfies the following differential equation:

$$\frac{\partial^2 m_y(z)}{dz^2} - k^2 m_y(z) + D_s = 0 \tag{7}$$

where $m_y(z)$ is the horizontal bending moment, and $k^2 = H y_c(z)/(hEI_y)$ is a variable coefficient accounting for the bending moment redistribution between deck and cables. $y_c(z)$ is the function describing the main cable sag measured from the tower top, h is the distance between tower top and girder, and EI_y represent the horizontal bending rigidity. According to equations (1) and (2), the projection of the horizontal bending moment in the perturbed configuration gives additional (second-order) terms affecting vertical and torsional equilibrium as geometric nonlinearities (figure 1b).

The aerostatic lift is considered in analogy with the dead load in the linearized deflection theory. Assuming that the corresponding vertical load is borne entirely by suspension cables and neglecting the cables' sag variation, the lift-induced stiffness degradation can be accounted for each value of wind speed by the definition of the horizontal cables tension due to the vertical load: $H = q_v l^2/(8f)$, with $q_v = q_g + L_s$. If $C_{l,0}$ is negative (for upward aerostatic lift) the horizontal tension in cables due to dead load decreases for increasing wind speeds. A validation of the simplifications introduced can be obtained by the application of the nonlinear deflection theory for high value of wind speed. For the benchmark case studies presented in Section 3, the assumptions made led to errors lower than 2% on the estimation of cables' sag and tension for $U = 100\ (m/s)$.

2.2. Multimodal framework

Letting the solutions of the system of equations (1) and (2) be: $v(z,t) = \bar{v}(z)e^{\lambda t}$ and $\vartheta(z,t) = \bar{\vartheta}(z)e^{\lambda t}$, the spatial functions are expressed by weighted sums of sinusoids having different wavelengths:

$$\bar{v}(z) = b\sum_{j=1}^{n} a_{v_j} \sin\left(\frac{j\pi z}{l}\right) \tag{8}$$

$$\bar{\vartheta}(z) = \sum_{k=1}^{m} a_{\vartheta_k} \sin\left(\frac{k\pi z}{l}\right) \tag{9}$$

Applying Galerkin method, an algebraic system of $N = n + m$ equations is obtained for the unknowns a_{v_j} and a_{ϑ_k}:

$$[A(\lambda, U)]\{a_{v,\vartheta}\} = \{0\} \tag{10}$$

Equation (10) represents a quadratic eigenvalue problem whose solution are the eigenvalues λ_r and eigenvectors $\{a_{v,\vartheta}\}_r$ identifying different vibration modes, with $r \in [1; 2N]$. The solution to equation (10) can be expressed as a linear combination of the 2N independent eigensolutions as:

$$V(x,t) = \sum_{r=1}^{2N} v_r(z) e^{\lambda_r t} \tag{11}$$

$$T(x,t) = \sum_{r=1}^{2N} \vartheta_r(z) e^{\lambda_r t} \tag{12}$$

where $v_r(z)$ and $\vartheta_r(z)$ are the vertical and torsional components of the r^{th} eigensolution, calculated by equations (8) and (9) for the various eigenvectors. Defining the pair of complex conjugate eigenvalues as $\lambda_r = \mu_r \pm i\omega_r$, and the corresponding eigenvector components in polar form $a_{v_{j,r}} = \left|a_{v_{j,r}}\right| e^{\pm i\Phi_{j,r}}$, $a_{\vartheta_{k,r}} = \left|a_{\vartheta_{k,r}}\right| e^{\pm i\Phi_{k,r}}$, equations (11,12) yield:

$$V(x,t) = \sum_{r=1}^{N} \left\{ 2e^{\mu_r t} \sum_{j=1}^{n} \left[\left|a_{v_{j,r}}\right| \sin\left(\frac{j\pi z}{l}\right) \cos\left(\Phi_{j,r} + \omega_r t\right) \right] \right\} \tag{13}$$

$$T(x,t) = \sum_{r=1}^{N} \left\{ 2e^{\mu_r t} \sum_{k=1}^{m} \left[\left|a_{\vartheta_{k,r}}\right| \sin\left(\frac{k\pi z}{l}\right) \cos\left(\Phi_{k,r} + \omega_r t\right) \right] \right\} \tag{14}$$

Hence, the vertical and torsional displacements are expressed as the sum of *r* modal contributions, each one being defined by the sum of *N* sine functions. The real part of the r^{th} pair of eigenvalues governs the exponential trend of the modal contribution, while the imaginary part represents the modal frequency. If the real part of an eigenvector is positive the system is unstable, having a divergent response with increasing time. The eigenvectors' imaginary parts describe the temporal shift between different contributions of the same mode as well as the phase-shift between different modes.

For each value of wind velocity, a complex eigenvalue analysis is performed to analyze the variation of natural frequencies and the respective modal shapes. The imaginary part of the first eigenvalue that violates the stability condition represents the critical frequency of the system. The corresponding wind velocity is the critical velocity.

3. Benchmark cases

Two suspension bridges are presented as case studies: the Yang-Sigang Bridge in China and the Çanakkale Bridge in Turkey. The Yang-Sigang Bridge is a double-deck truss girder bridge, with a main span of 1700 meters and two side spans of 468 meters. It is currently the world's longest span

double-decked bridge, and the third among all, after the Çanakkale Bridge and the Akashi Kaikyo Bridge. The Çanakkale Bridge is a twin-box girder bridge, with the world's longest span of 2023 meters and 770 meters side spans. Some of the main structural features of the two bridges are summarized in Table 1. Geometric and mass data were taken from [3] and [4] respectively for Yang-Sigang Bridge and Çanakkale Bridge, while moments of inertia (I_x and I_y), and torsional modulus (I_t) were calculated by fitting structural frequencies. The aeroelastic analysis was performed for the selected cases, and the evolution of structural frequencies and modal shapes with increasing wind speed was investigated. Eight sinusoids were chosen to describe both vertical and torsional displacement components: $n = m = 8$ in equations (8) and (9). Therefore, sixteen modes were included in the analysis but, for the sake of brevity, only results relative to first eight modes will be illustrated in following sections. In the next subsections, mode labels are sorted for ascending order of frequency, that is "mode *r*" refers to the vibration mode associated to the r^{th}-lowest frequency.

Steady-state aerodynamic coefficients are: $C_{l,0} = 0.01$ (downward) and $C_{d,0} = 0.9$ for the Yang-Sigang Bridge [3]; $C_{l,0} = 0.058$ (downward) and $C_{d,0} = 0106$ for the Çanakkale Bridge [4]. Flutter derivatives of the cross-sections, given in [5] and [6] for Yang-Sigang and Çanakkale Bridge, respectively, are plotted in figures 2 and 3.

Table 1. Main features of the analyzed case studies.

	l (m)	b (m)	f (m)	μ_g (t)	I_ϑ (tm^2/m)	I_x (m^4)	I_y (m^4)	I_t (m^4)
Yang-Sigang	1700	14	228	53.072	7466	25	137.8	46
Canakkale	2023	19.5	188.9	28.853	6200	5.8	419	14

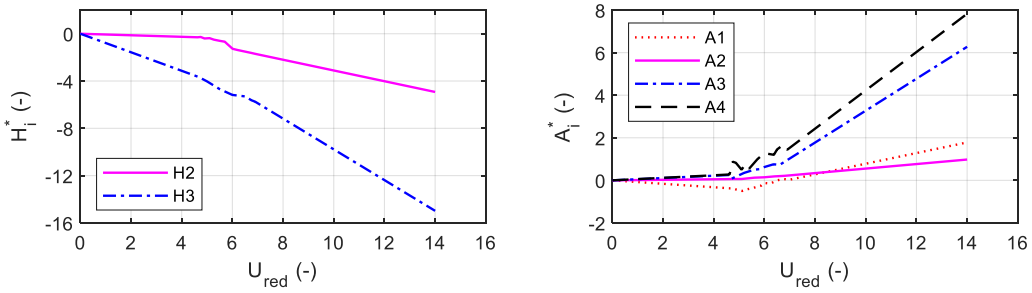

Figure 2. Flutter derivatives of Yang-Sigang Bridge.

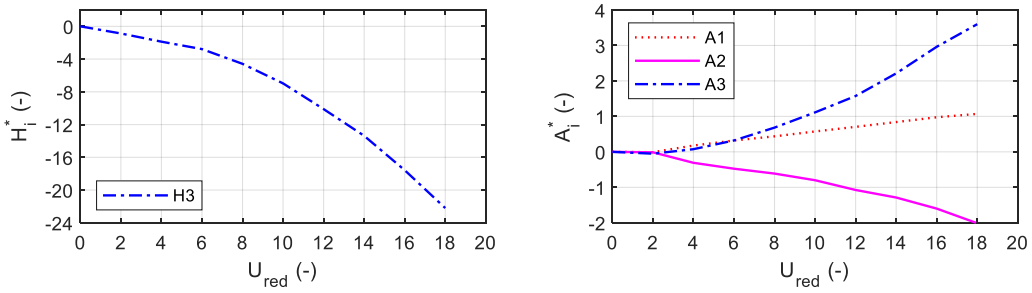

Figure 3. Flutter derivatives of Çanakkale Bridge.

3.1. Yang-Sigang Bridge

To investigate the effect of aerostatic nonlinearities, two different analyses were performed, where the aerostatic load was ignored (case *a*) and included (case *b*). The variation of modal frequencies and damping factors for increasing wind speed is shown in figures 4 and 5 for cases *a* and *b*, respectively.

For the sake of brevity, modal shapes are only illustrated for the free-wind condition (figure 6) and for the critical condition corresponding to the flutter onset of case *b* (figure 7). Results show that wind speed affects only modal shape and frequency of the torsional symmetric mode. The real part of the corresponding eigenvalue sharply increases after the crossing between modes 6 and 7 and becomes positive at the critical wind speed of 50.85 m/s, denoting a hard-type flutter. The limit threshold is in line with the prediction of [5], where a flutter velocity of 51 m/s is found, when a structural damping ratio of 0.52% is considered.

The flutter modal shape (figure 7, mode 6) is almost purely torsional, having a minor flexural component, as usual for SDOF torsional flutter. The occurrence of a SDOF torsional flutter could also be predicted by the sign of the A_2^* flutter derivative (figure 2). Aerostatic-induced nonlinearities have a minor influence in this case, where the non-stationary load leads a hard-type damping-driven instability at a relatively small wind speed.

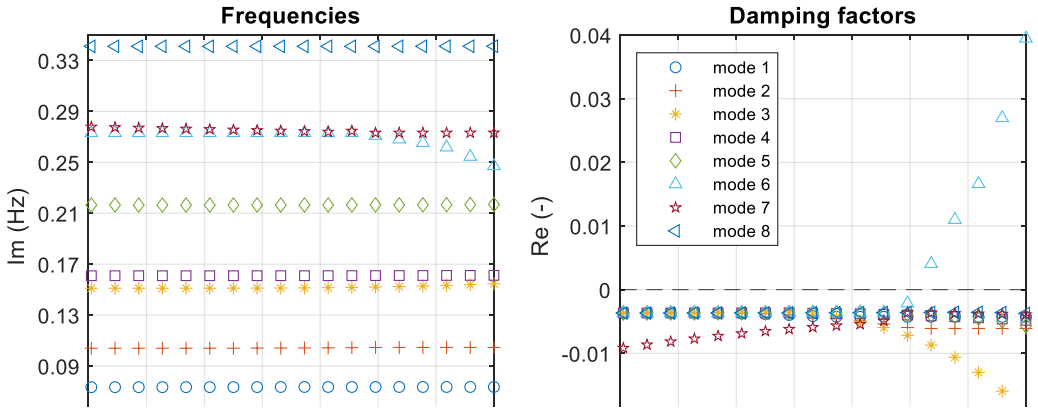

Figure 4. Modal frequencies and damping factors of Yang-Sigang Bridge (Case *a*).

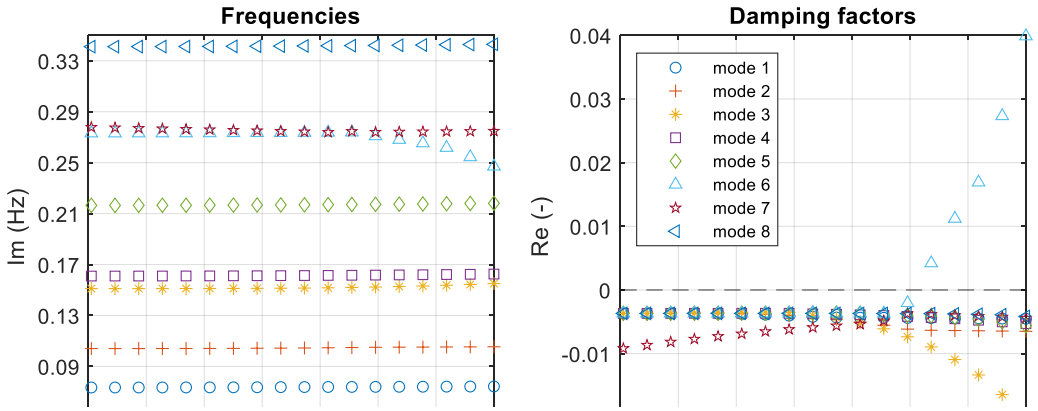

Figure 5. Modal frequencies and damping factors of Yang-Sigang Bridge (Case *b*).

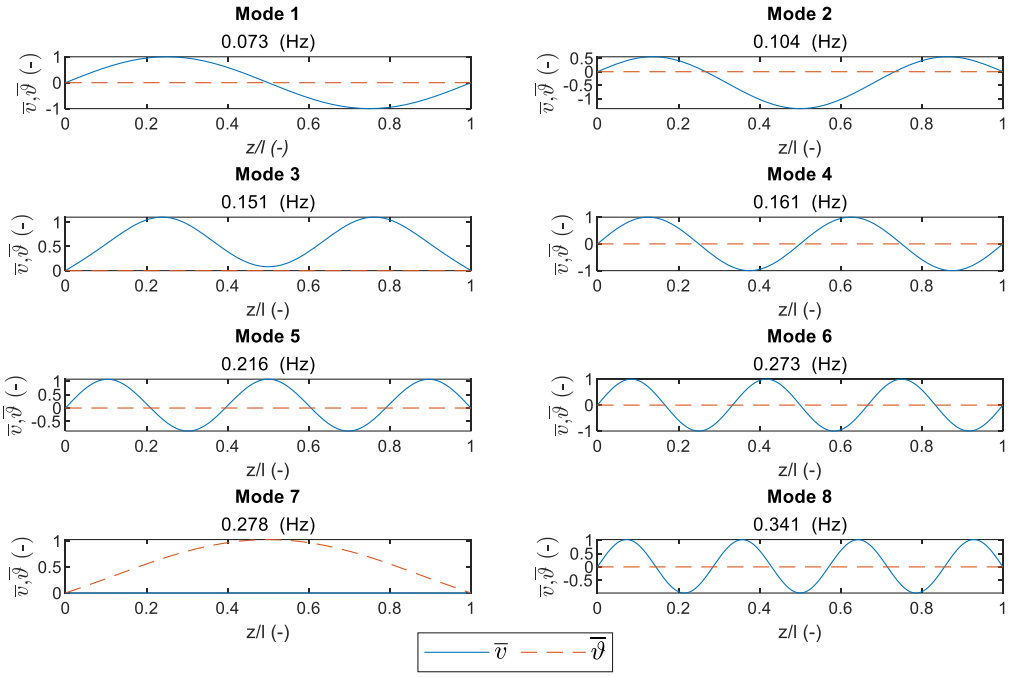

Figure 6. Yang-Sigang Bridge modal shapes in the free-wind condition.

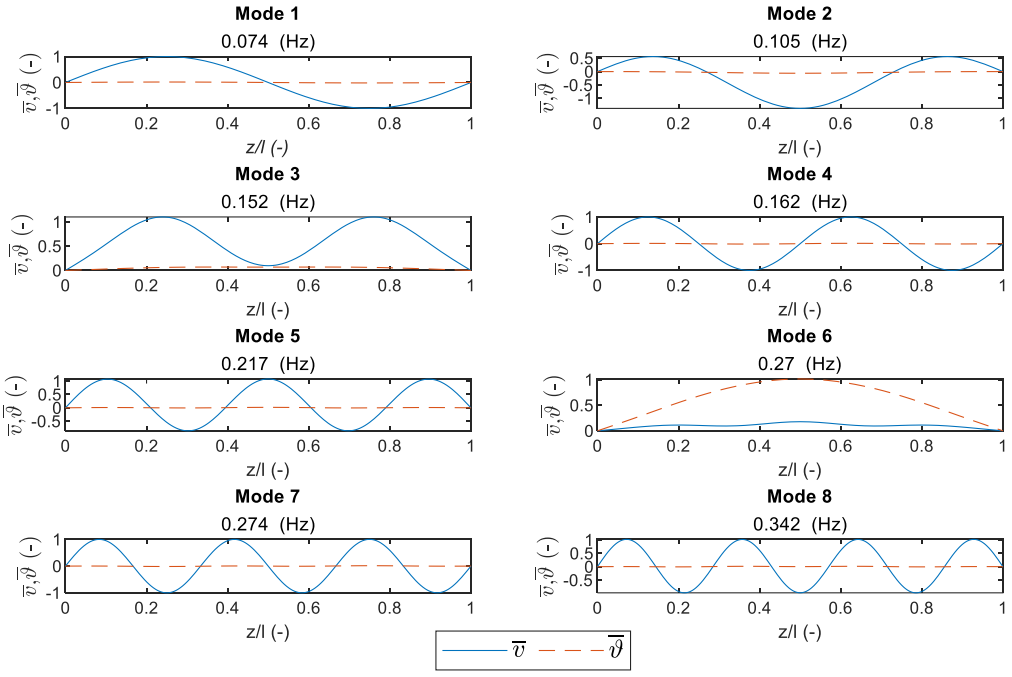

Figure 7. Yang-Sigang Bridge modal shapes in the critical flutter condition of case *b*.

3.2. Çanakkale Bridge

In analogy with previous case study, the Çanakkale Bridge was analyzed ignoring (case *a*) and including (case *b*) aerostatic load components. Figures 8 and 9 illustrate the variation of modal frequencies and damping factors for increasing wind speed for cases *a* and case *b*, respectively. Figures 10 and 11 show the modal shapes for the free-wind condition and critical condition of case *b*.

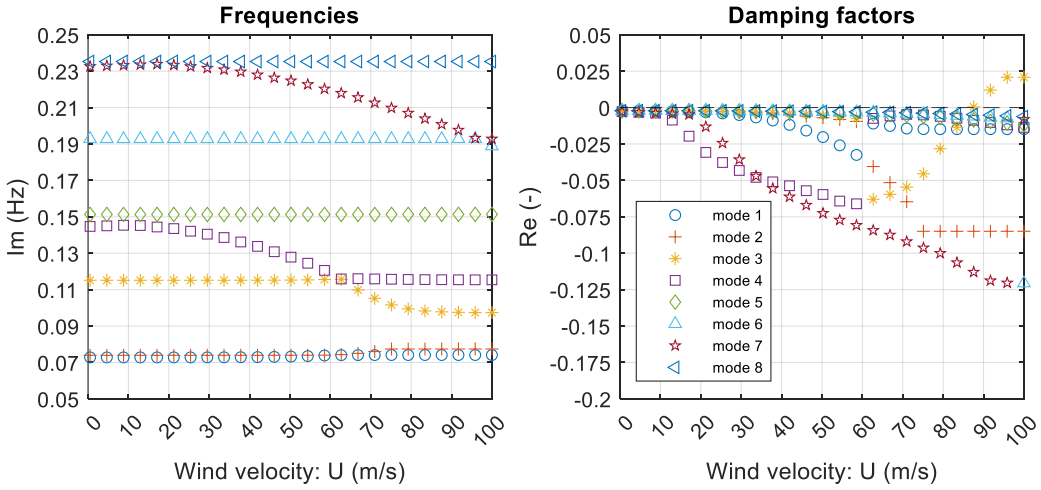

Figure 8. Modal frequencies and damping factors of Çanakkale Bridge (Case *a*).

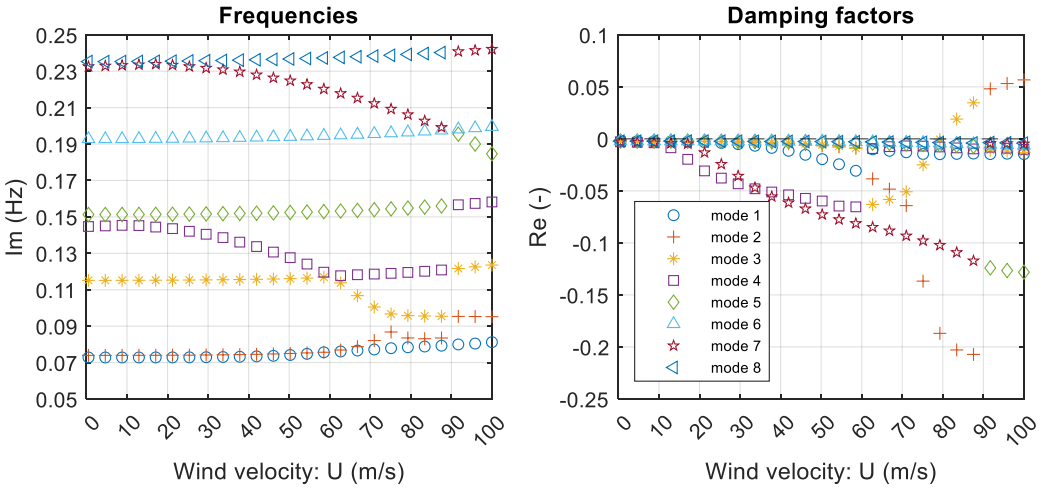

Figure 9. Modal frequencies and damping factors of Çanakkale Bridge (Case *b*).

In this case, aerostatic induced non-linearities have a remarkable influence on the flutter treshold, which is 89 m/s for case *a*, and 78.7 m/s for case *b*. The results obtained are consistent with the ones in [6], which report a flutter wind speed of 89.79 m/s for a 0° angle of attack and 78.84 for a –3° angle of attack. Nevertheless, for a better comparison, a more refined analysis considering the aerostatic-induced span-wise variation of flutter derivatives should be performed. Worth noting that drag force redistribution between deck and cables modelled by equation (7), plays an important role in the aeroelastic response. If the drag force is assumed to be borne entirely by the deck-girder, i.e. the horizontal bending moment in the deck – considered as a simply supported beam of length l loaded by the constant transverse load D_s – is given by $m_y(z) = D_s z(l-z)/2$, then a flutter critical wind speed of 66 m/s is obtained.

In both cases *a* and *b*, flutter instability can be ascribed to the interaction between the first symmetric vertical and torsional modes: modes 1 and 4 in the free-wind condition (figure 10), which cross the adjacent modal branches becoming modes 2 and 3 at the flutter onset (figure 11). The torsional branch's damping ratio starts growing at 60 m/s and becomes positive at 78.8 m/s, after crossing the vertical branch's damping ratio, in corrispondence to the veering of the relevant modal frequencies. The interaction between symmetric vertical and torsional displacement components of the

flutter mode is illustrated in figure 12 from the mode shape perspective. The vertical component of the symmetric torsional-bending mode grows for increasing wind speed, the resulting flutter mode is flexural-torsional, as is usual for the coupled-mode, stiffness-driven flutter instability.

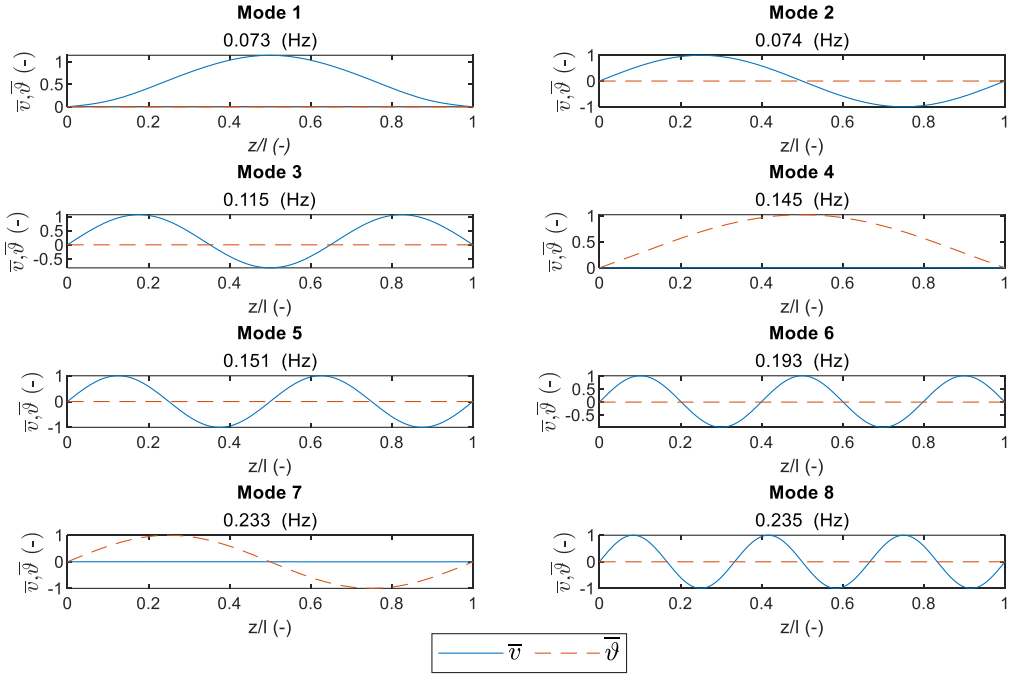

Figure 10. Çanakkale Bridge modal shapes in the free-wind condition.

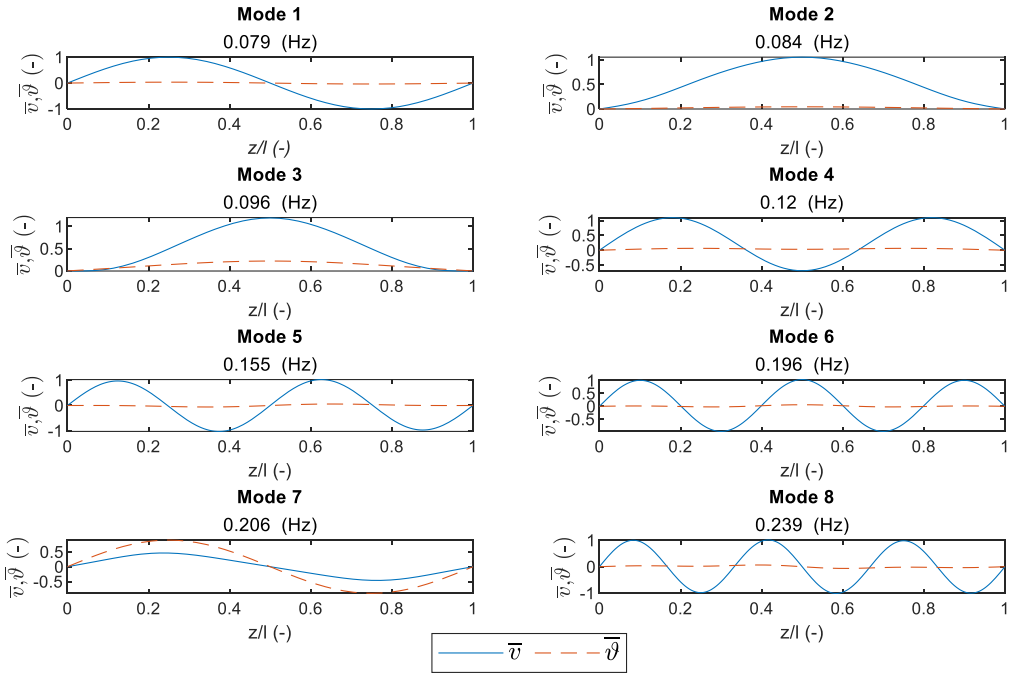

Figure 11. Çanakkale Bridge modal shapes in the critical flutter condition of case *b*.

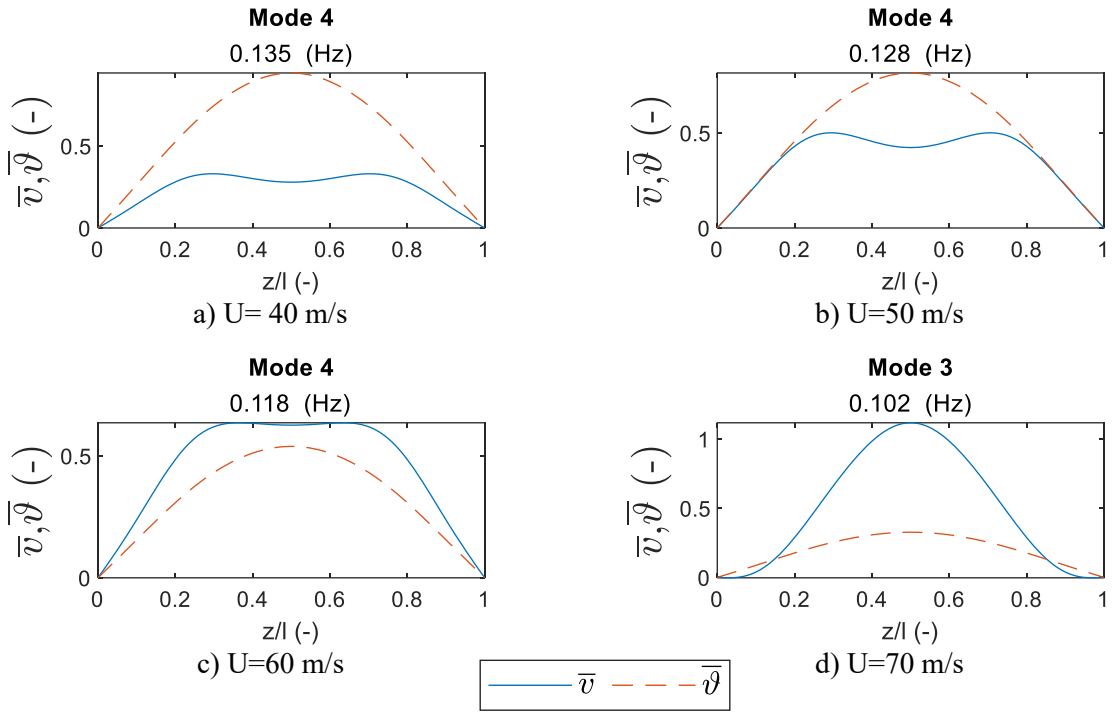

Figure 12. Vertical and torsional components of the critical flutter mode at different wind speeds.

4. Conclusion

A semi-analytic model for the multi-modal aeroelastic analysis of suspension bridges including aerostatic nonlinearities was presented. The variation of the bridge mode shapes and frequencies for increasing values of wind speed was discussed. Flutter wind velocities provided for the selected case studies are consistent with literature data. Some peculiar features of stiffness-driven and damping-driven flutter instability were highlighted in the proposed framework. The wind-induced geometric nonlinearities investigated were found to have a remarkable influence on the stiffness-driven flutter instability of Çanakkale Bridge, and a negligible effect on the damping-driven flutter of Yang-Sigang Bridge.

References

[1] Piana G and Carpinteri A 2021 Long-span Suspension Bridge Flutter Analysis with Drag Force Effects *Journal of Applied and Computational Mechanics* **7** 1077–89
[2] Scanlan R H and Tomko J J 1971 Airfoil and Bridge Deck Flutter Derivatives *Journal of the Engineering Mechanics Division* **97** 1717–37
[3] Li M, Sun Y, Lei Y, Liao H and Li M 2021 Experimental Study of the Nonlinear Torsional Flutter of a Long-Span Suspension Bridge with a Double-Deck Truss Girder *International Journal of Structural Stability and Dynamics* **21** 2150102
[4] Ronne M, Larsen A and Walther J H 2021 The nose up effect in twin box bridge deck flutter: Experimental observations and theoretical model *Wind and Structures* **32** 293–308
[5] Wu B, Chen X, Wang Q, Liao H and Dong J 2020 Characterization of vibration amplitude of nonlinear bridge flutter from section model test to full bridge estimation *Journal of Wind Engineering and Industrial Aerodynamics* **197** 104048
[6] Liao H, Wang Q, Zhu J, Ren T and Shao C 2022 Flutter instability of 1915 Canakkale Bridge Considering Nonlinear Aero-static Effect. *8th European-African Conference on Wind Engineering*